ACS OMEGA

http://pubs.acs.org/journal/acsodf

Article

Synergistic Mechanism of Combined Inhibitors on the Selective Flotation of Arsenopyrite and Pyrite

Xiaohao Sun, Bozeng Wu,* Jiushuai Deng,* Hongxin Qiu,* Mingzhen Hu, Jiaozhong Cai, Xiaoli Jin, and Hongyang Xu

Cite This: *ACS Omega* 2022, 7, 6302−6312

Read Online

ACCESS | Metrics & More | Article Recommendations

ABSTRACT: The selective action mechanism of sodium butyl xanthate (BX), ammonium salt (NH_4^+), and sodium *m*-nitrobenzoate (m-NBO) on pyrite and arsenopyrite was examined by experiments and quantum chemistry. The experiments show that under alkaline conditions, ammonium salt (NH_4^+) and m-NBO can have a strong inhibitory effect on arsenopyrite. At pH 11, the recovery rate of arsenopyrite reduces to 16%. The presence of ammonium salt (NH_4^+) and m-NBO reduces the adsorption energy of BX on arsenopyrite to $\Delta E = -23.23$ kJ/mol, which is far less than the adsorption energy on the surface of pyrite, $\Delta E = -110.13$ kJ/mol. The results are helpful to understand the synergistic mechanism of the agent on the surface of arsenopyrite and pyrite, thus providing a reference for the selective separation of arsenopyrite.

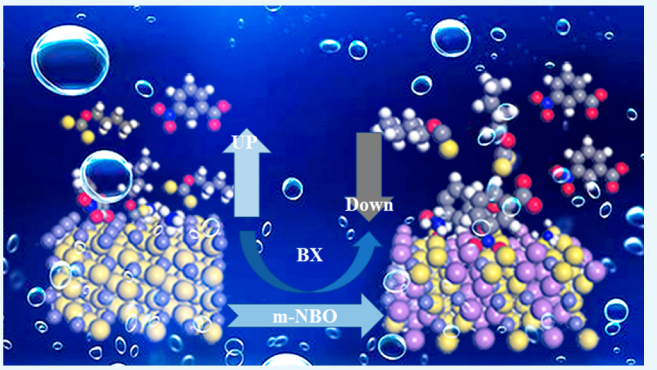

1. INTRODUCTION

Arsenopyrite (FeAsS) is an extensively distributed mineral that commonly coexists with other sulfides. A major limitation with the treatment of As-containing polymetallic sulfide ores is that the As content in the concentrate product is too extremely high. This is because the formation conditions and crystal structure of arsenopyrite and other sulfide minerals such as pyrite (FeS_2) are roughly similar;[1] hence, their physical and chemical properties are also extreme. Therefore, using conventional flotation reagents causes arsenopyrite and pyrite to be collected together, which in turn makes the As content in the pyrite concentrate significantly exceed the standard. This increases the smelting costs, reduces the value of the sulfide minerals' concentrate, and causes serious environmental pollution.[2] The inorganic arsenate and As-containing organic matter generated by the oxidation of As-containing minerals can pollute the environment and affect human health via the grand geological cycle and minor biological cycle.[3] Beneficiation technology is commonly used before smelting to minimize the As content in nonferrous metal sulfide concentrates and treat the separated As-containing products.[4] It is important to improve the production efficiency and environmental protection.[5]

Many domestic and foreign researchers examined the technologies and principles of separating pyrite and arsenopyrite. Flotation is extensively used and can be classified in four types: heating flotation, oxidants,[6] electrochemical oxidation,[7] and inhibitors.[8] The increased processing volumes of As-containing sulfides and stringent quality requirements for concentrates increased the prominence of inhibitors, which can be divided in two categories: inorganic[9] and organic.[10] The mechanism of inorganic inhibitors is well understood. In general, two or more inhibitors are used to enhance the inhibitory effect. Compared with inorganic inhibitors, organic inhibitors offer many types of features, no pollution and a wide range of sources. Inhibitors can be combined with different agents to strengthen their effectiveness and selectivity.[11] Although researchers have extensively focused on arsenopyrite and pyrite, they have also focused on novel inhibitors or compound inhibitors, while there is less research on the combined synergy between inorganic and organic agents. In particular, the understanding of the interaction mechanism between them is not deep enough. However, the increasingly stringent requirements for environmental protection have caused researchers to focus on developing novel effective and nontoxic combinations of inhibitors and reagents. Thus, inorganic and organic inhibitors are combined for selective

Received: December 6, 2021
Accepted: January 31, 2022
Published: February 10, 2022

https://doi.org/10.1021/acsomega.1c06902
ACS Omega 2022, 7, 6302−6312

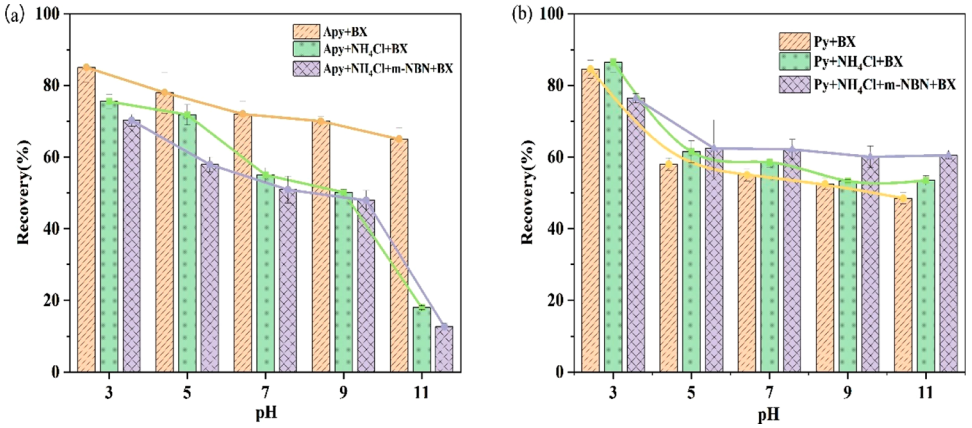

Figure 1. Effect of pH on the recovery of (a) Apy and (b) Py when using BX, NH_4^+, and m-NBO; $C_{(BX)} = 1.6 \times 10^{-3}$ mol/L.

separation of arsenopyrite and other sulfides, which has become the focus of future research.[12] This has led to a trend of increasingly complex flotation reagents.

The synergy between different reagents has an extremely complex mechanism, and little theoretical research on this topic has been reported. Experimental studies demonstrated that the mechanism may be related to chemical combination, chelation, and adsorption.[13,14] Xanthates are excellent collectors owing to the special affinity between the metal atoms of the mineral and the chelating reagent, which in turn leads to a chemical reaction between the collector and mineral. Inhibitors primarily chelate with metal atoms or promote their oxidation, thus forming a passivation film on the mineral surface. However, the competitive adsorption of combined reagents indicates that a reagent adsorbed on the mineral surface may interact with the accompanying inhibitor, and their mutual effects on each other may ultimately promote and strengthen the flotation process.[15] The synergistic effect has been applied to the flotation of Cu ores; for example, Sherwood Copper processes a high-grade Cu−Au deposit at Minto Mine in Yukon, Canada. However, the mechanism of combined reagents is unclear, and the interaction between inorganic and organic inhibitors requires additional study. Janetski et al.[16] performed flotation experiments on sulfides; however, certain limitations still cannot be explained by empirical results. The flotation mechanism needs to be clarified at the microscale to explain the influence of chemical reagents on minerals during the flotation process.[17−20] The emergence of quantum chemistry has thus made such a clarification possible.[21]

This study examined the effects of different reagents on the flotation of arsenopyrite and pyrite. Microflotation experiments, zeta potential measurements, Fourier transform infrared spectroscopy (FTIR), and molecular simulation were performed to analyze the mineral surface before and after the action of each reagent. The results of this study should provide theoretical guidance for separating arsenopyrite and pyrite by flotation.

2. RESULTS AND DISCUSSION

2.1. Microflotation Experiment. Figure. 1 shows the effects of the collector sodium butyl xanthate (BX), inhibitor *m*-nitrobenzoate (m-NBO), and activating reagent NH_4^+ on the floatability of arsenopyrite (Apy) and pyrite (Py) depending on pH. When BX was used itself, Apy demonstrated good floatability under acidic conditions, and its floatability decreased with increase in pH. Unlike its effect on Py, NH_4^+ has an inhibitory effect on Apy;[22] therefore, its addition reduced the floatability of Apy in the studied pH range. The addition of the inhibitor m-NBO decreased the floatability of Apy under alkaline conditions. Moreover, Py demonstrated good floatability under acidic conditions when BX was used alone. Increasing the pH significantly reduced the floatability of Py. With m-NBO, Py demonstrated good floatability for the entire pH range with a recovery rate of >60% regardless of pH. The addition of NH_4^+ reduced the effect of m-NBO on Py. When the mass concentration of m-NBO was 50 mg/L, the flotation recovery rate was >60%. This shows that pH had little effect on the recovery rate of Py when NH_4^+ was added. Note that the inhibitor m-NBO had no effect on the flotation of Py when NH_4^+ was added. In summary, addition of NH_4^+ reduced the inhibitory effect of m-NBO on Py, which retained good floatability throughout the studied pH range. However, the addition of m-NBO after NH_4^+ reduced the floatability of Apy under alkaline conditions. When NH_4^+ reacted with m-NBO, the inhibitor was selectively adsorbed on the Apy surface. Moreover, m-NBO and BX competed to adsorb on the Apy surface, which reduced the floatability of Apy. However, the Py surface was protected by NH_4^+, which weakened the adsorption of m-NBO.

When the NH_4^+ concentration was fixed, Figure. 2 shows that increase in the m-NBO concentration affected the flotation recovery of Apy and Py. When the combined inhibitor concentration reached [NH_4^+ + m-NBO] = 75 mg/L + 75 mg/L (molar ratio of 3.5:1), the difference in the flotation recovery rates of Py and Apy was maximized. The increase in m-NBO concentration gradually increased the flotation recovery rate of Py, which stabilized at ∼60%. The increase in the m-NBO concentration initially decreased the flotation recovery of Apy, which then gradually stabilized at ∼18%. These results demonstrate that NH_4^+ and m-NBO can be combined to realize the selective flotation of Py and Apy.

Flotation separation experiments were performed on pyrite-toxin sand artificial mixed ore using single-agent m-NBO and combination agent [NH_4^+ + m-NBO], and the results are shown in Figure 3. Figure 3(a) shows that single-agent m-NBO pyrite and arsenopyrite concentrate, with a grade of 48.14% S and 1.60% As and recovery rates of 74.32% S and 20.26% As, was obtained, compared with the obtained tailings containing 29.72% S and 11.18% As, with recovery rates of 25.68% S and 79.74% As. Under the [NH_4^+ + m-NBO] combination agent, as shown in Figure 3(b), the concentrate grades were as

https://doi.org/10.1021/acsomega.1c06902
ACS Omega 2022, 7, 6302−6312

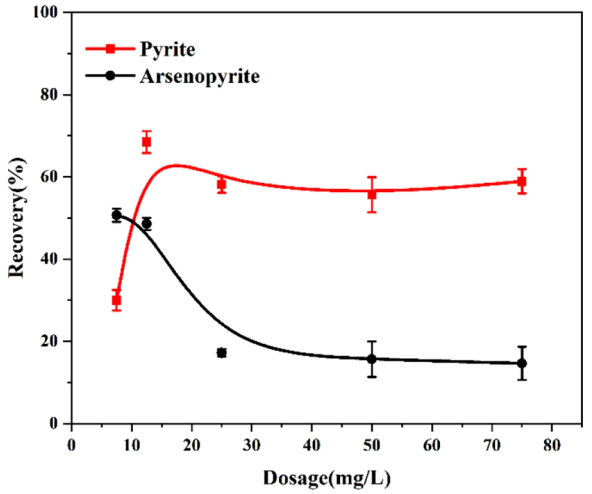

Figure 2. Effect of the inhibitor concentration (m-NBO) on the flotation recovery of Py and Apy; $C_{(BX)} = 1.6 \times 10^{-3}$ mol/L, $C(NH_4^+)$ = 75 mg/L.

follows: 35.77% S and 1.00% As, with recoveries of 52.06% S and 10.92% As, respectively; nevertheless, the obtained sand contained 37.21% S and 7.15% As, with recovery rates of 47.94% S and 86.33% As, respectively. Therefore, the combination inhibitor can be used to separate pyrite and thus poison sand.

2.2. Zeta Potential Analysis. Figure 4 shows the zeta potentials of Apy and Py surfaces before and after interaction with BX. In the absence of BX, the isoelectric points (IEPs) of Apy and Py were 3.96 and 7.99, respectively. When pH < IEP, the Apy and Py surfaces were positively charged, and BX electrostatically adsorbed on the mineral surface. When pH > IEP, the Apy and Py surfaces were negatively charged, and it was difficult for BX to adsorb on the mineral surface. The interaction with BX greatly promoted a positive shift in the zeta potentials of Apy and Py. This indicates that BX significantly affected the surface properties. There was little difference between the zeta potentials of Apy and Py, which indicates that BX affected the floatabilities of Apy and Py in a similar manner.

When Apy interacted with BX, the zeta potential of the Apy surface decreased for the entire pH range. In this study, the mineral surfaces generally had a negative zeta potential, which indicates that the collector and Apy surface primarily interacted via chemical adsorption with certain electrostatic adsorption. When Py interacted with BX, the zeta potential of the Py surface decreased for the entire pH range. This indicates that the negatively charged BX adsorbed on the mineral surface.

Figure 5 shows the zeta potentials of the Apy and Py surfaces under the combined effects of NH_4^+ and m-NBO. The combined inhibitor promoted the positive movement of the zeta potential. For Apy, the IEP moved to pH 4.48 with NH_4^+ and 4.31 with NH_4^+ and m-NBO. For Py, the IEP moved to 8.52 with NH_4^+ and 7.89 with NH_4^+ and m-NBO. This indicates that combining NH_4^+ and m-NBO had considerable effect on the mineral surface properties. The zeta potentials of Apy and Py demonstrated important differences after treatment with NH_4^+ and m-NBO, particularly at pH 8−12, which can help explain their different flotation performances in microflotation experiments. The addition of NH_4^+ decreased the zeta potential of Apy considerably more than that of Py, which indicated that NH_4^+ has a much greater affinity with Apy than with Py. Subsequently, the addition of m-NBO significantly reduced the zeta potential of Apy compared with Py. This may be explained by the formation of a strong passivation layer on the Apy surface; it reduced the adsorption of the collector BX and inhibited the flotation recovery of Apy. Howevery, NH_4^+ had a protective effect on Py,[23] which weakened the adsorption of m-NBO and caused the Py surface to adsorb a considerably greater amount of the collector BX. This enhanced the floatability of Py even in the presence of m-NBO; therefore, the greatest inhibition of Apy in the microflotation test coincided with the conditions for a considerable decrease in the zeta potential.

2.3. FTIR Analysis. Figure 6 and Table 1 show the IR spectra and characteristic peaks of the Apy surface before and after its interaction with NH_4^+, m-NBO, and BX. Apy had a broad reflection peak close to 1630 cm^{-1} and a weak absorption peak at 1069 cm^{-1}. After the action of BX, new absorption peaks appeared at 1112 cm^{-1} (ref 24) and 1382 cm^{-1}; these peaks are characteristic of BX and indicate that BX adsorbed on the Apy surface. After the action of NH_4^+, a novel characteristic peak appeared at 1381 cm^{-1}.[25] When BX was added, the characteristic peak of BX at 1112 cm^{-1} did not appear in the IR spectrum, which can be attributed to competitive adsorption. The peak at 1381 cm^{-1} corresponds to NH_4^+ and indicates that the adsorption of BX onto the Apy surface was extremely weak. Therefore, NH_4^+ caused changes to the surface potential of the Apy surface. Xanthate oxidizes to dixanthate and xanthate, which appear on the IR spectrum at

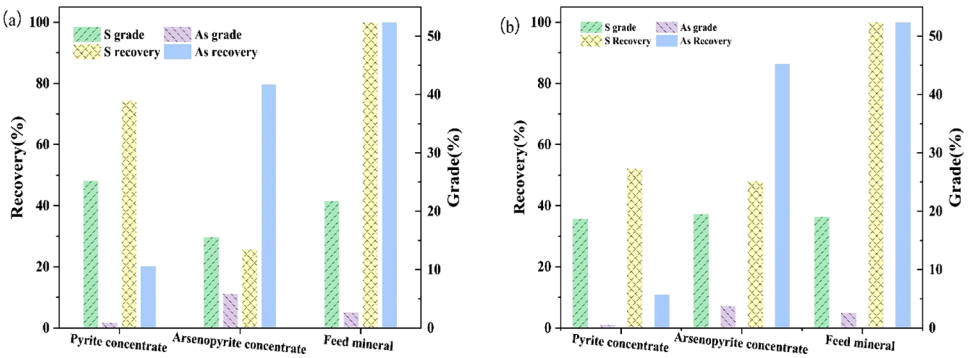

Figure 3. Flotation separation results of the pyrite−arsenopyrite artificial mixed minerals: (a) flotation separation of single-agent m-NBO pyrite and arsenopyrite concentrate; (b) flotation separation of combination agent [NH_4^+ + m-NBO] pyrite and arsenopyrite concentrate.

https://doi.org/10.1021/acsomega.1c06902
ACS Omega 2022, 7, 6302−6312

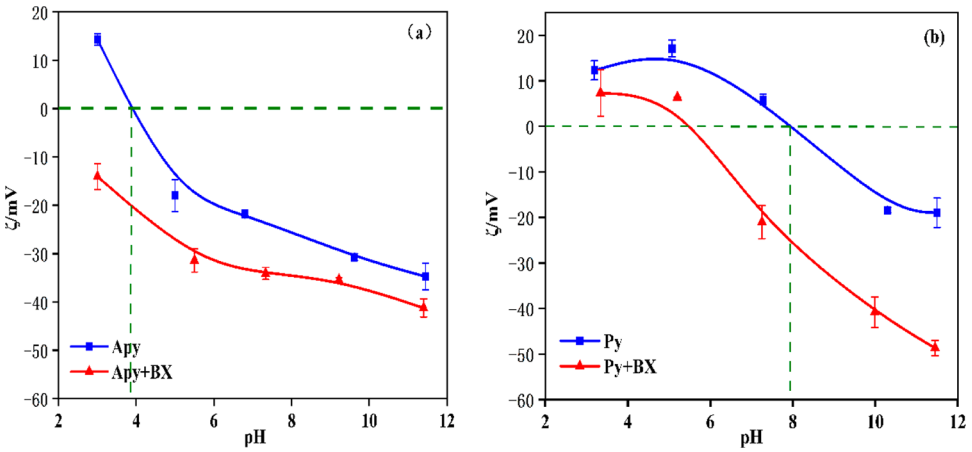

Figure 4. Relationships between the zeta potential and pH before and after the action of BX: (a) Apy and (b) Py.

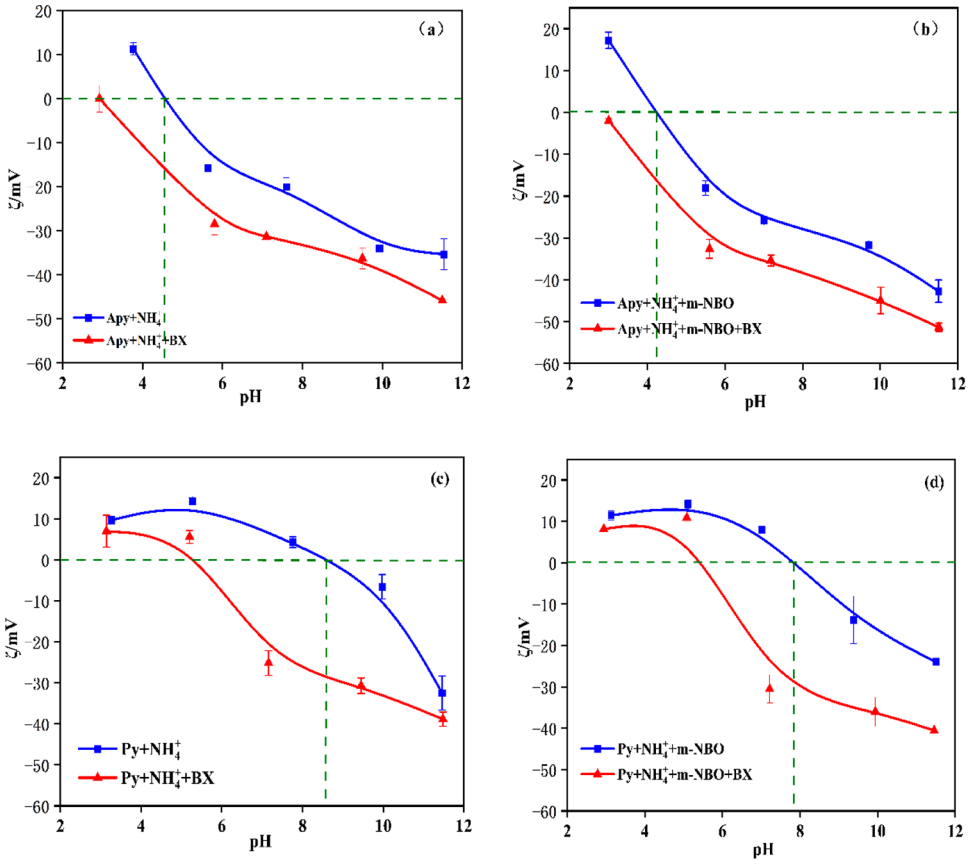

Figure 5. Relationships between the zeta potential and pH before and after the actions of NH_4^+ and m-NBO: (a) Apy before and after NH_4^+; (b) Apy and NH_4^+ before and after m-NBO; (c) Py before and after NH_4^+; (d) Py and NH_4^+ before and after m-NBO.

1112 cm^{-1} (ref 24) and 1382 cm^{-1}. The absorption peaks in the IR spectrum are characteristic of dixanthate and xanthate, which indicates that these may be the effective flotation components for Apy after the action of NH_4^+ and BX. After the action of m-NBO, there was no obvious change in the characteristic peaks of the IR spectrum, which may be attributed to the elimination of the absorption peak of m-NBO itself at 1377 cm^{-1}.

Figure 7 and Table 2 show the IR spectra and characteristic peaks of the Py surface before and after its interaction with NH_4^+, m-NBO, and BX. After the action of BX, novel absorption peaks were observed at 1094 and 1382 cm^{-1}, which are characteristic of xanthate and dixanthate and indicate that BX adsorbed on the Py surface.[26] After the action of NH_4^+, a novel absorption peak was observed at 1382 cm^{-1}.[25] After the combined action of NH_4^+ and BX, a novel absorption peak was observed at 1090 cm^{-1}, which indicates the adsorption of dixanthate and xanthate on the Py surface. After adding m-NBO after the action of NH_4^+, the IR spectrum retained the above-mentioned characteristic absorption peaks. The absorption peak at 1382 cm^{-1} can be attributed to the combined effect of NH_4^+ and m-NBO. The addition of BX caused a new IR absorption peak to appear at 1101 cm^{-1} and a weaker absorption peak to appear at 1379 cm^{-1}. These results show

https://doi.org/10.1021/acsomega.1c06902
ACS Omega 2022, 7, 6302−6312

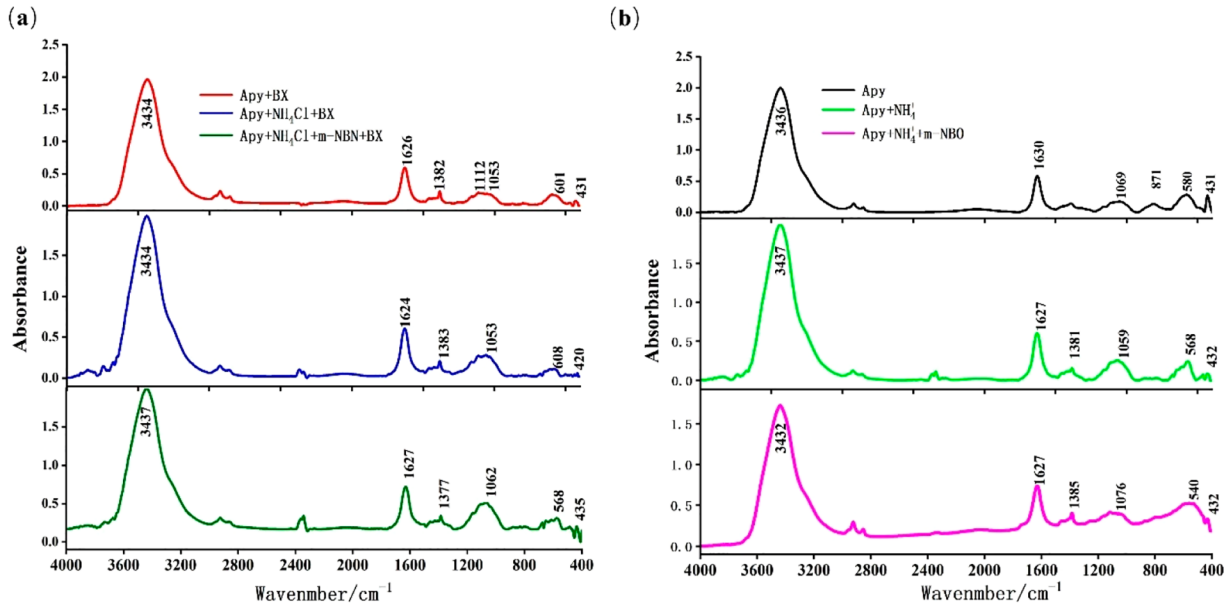

Figure 6. Infrared spectra of Apy before and after the actions of NH_4Cl, m-NBO, and BX: (a) with BX and (b) without BX.

Table 1. Characteristic Peaks for the IR Spectrum of Apy and the Effects of the Flotation Reagents

Wavenumber (cm^{-1})							
Apy	Apy + BX	Apy + NH_4^+	Apy + NH_4^+ + BX	Apy + NH_4^+ + m-NBO	Apy + NH_4^+ + m-NBO + BX	Functional groups	Bonding properties
3436	3434	3437	3434	3432	3437	O−H bending vibrations	water (adsorbed water)
1630	1626	1627	1624	1627	1627	O−H bending vibrations	water (adsorbed water)
				1385	1377	-NO_2 symmetrical stretching vibration	m-NBO
		1381				Inorganic ammonium ion	NH_4^+
	1382		1383			-CH_3 bending vibrations	NaBX
	1112					C═S stretching vibration	NaBX
1069	1053	1059	1053	1076	1062	SO_4^{2-} stretch vibration	Apy
871						As−O stretching vibration	Apy
580	601	568	608	540	568	Fe−O stretching vibration	Apy
431	431	432	420	432	435	O−As−O bending vibrations	Apy

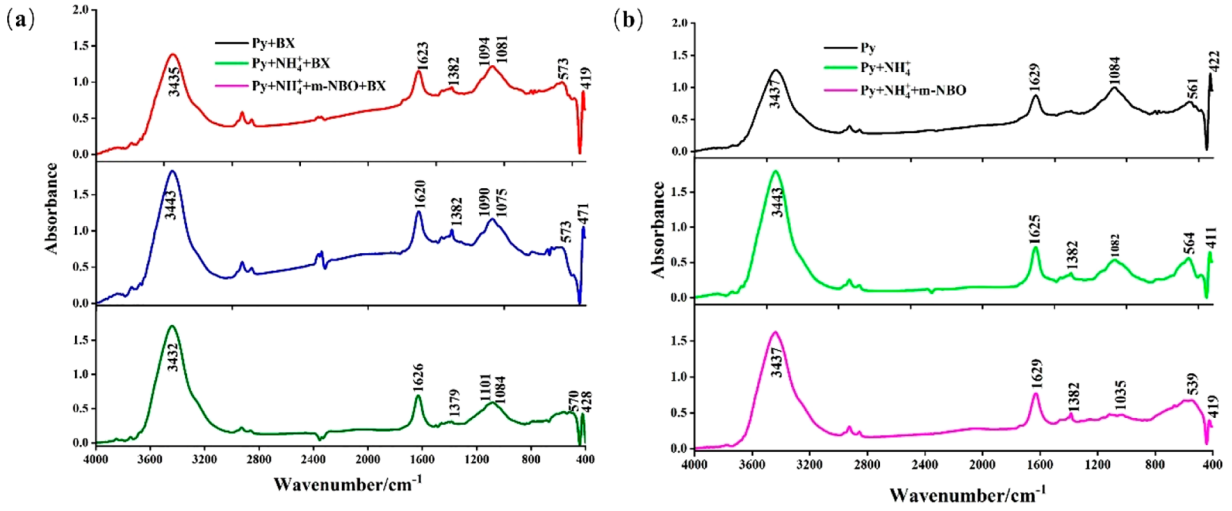

Figure 7. Infrared spectra of Py before and after the actions of NH_4Cl, m-NBO, and BX: (a) with BX and (b) without BX.

that the effect of m-NBO on Py was reduced because of competitive adsorption among flotation reagents.[27]

2.4. Quantum Chemical Analysis. *2.4.1. Frontier Orbital Analysis.* The frontier orbital shape and composition of a

https://doi.org/10.1021/acsomega.1c06902
ACS Omega 2022, 7, 6302−6312

Table 2. Characteristic Peaks for the IR Spectrum of Py and the Effects of Flotation Reagents

Wavenumber (cm^{-1})							
Py	Py + BX	Py + NH_4^+	Py + NH_4^+ + BX	Py + NH_4^+ + m-NBO	Py + NH_4^+ + m-NBO + BX	Functional groups	Bonding properties
3437	3435	3443	3443	3437	3432	O−H bending vibrations	water (adsorbed water)
1629	1623	1625	1620	1629	1626	O−H bending vibrations	water (adsorbed water)
				1382	1379	-NO_2 symmetrical stretching vibration	m-NBO
		1382				Inorganic ammonium ion	NH_4^+
	1382		1382			-CH_3 bending vibrations	BX
	1094		1090		1101	C═S stretching vibration	BX
1084	1081	1082	1075	1035	1084	SO_4^{2-} stretch vibration	Py
561	573	564	573	539	570	Fe−O stretching vibration	Py
422	419	411	471	419	428	O−Fe−O bending vibrations	Py

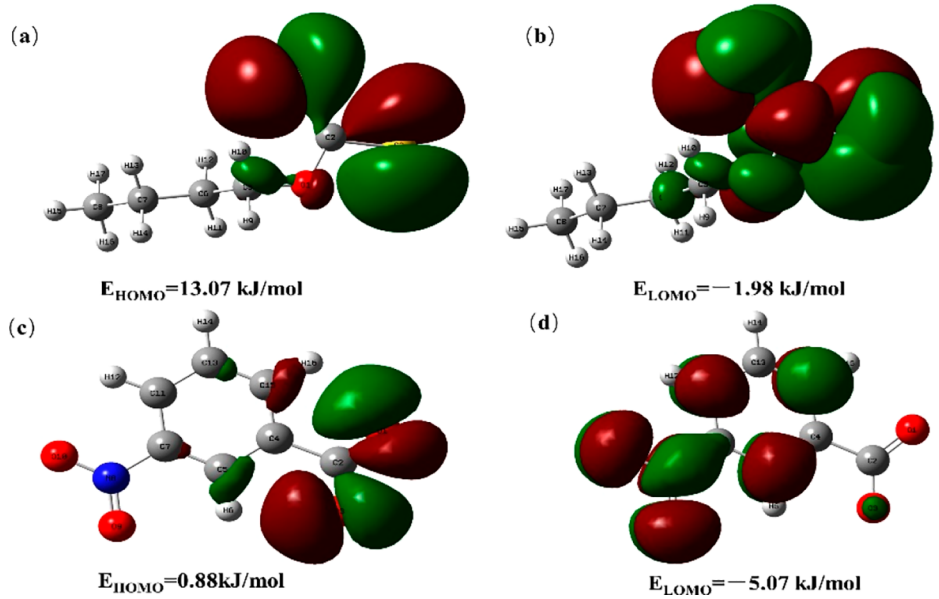

Figure 8. Frontier orbitals for the molecular structures of the flotation reagents: (a) HOMO and (b) LUMO of BX; (c) HOMO and (d) LUMO of m-NBO.

flotation reagent can be used to intuitively show which atom is possibly the active site of a reaction. To facilitate a qualitative understanding of the atomic contributions of BX and m-NBO, Figure 8 shows the frontier orbitals of their molecular structures. The parameters are presented in Table 3. E_{HOMO} and E_{LUMO} are the energies of the highest occupied molecular orbital (HOMO) and lowest unoccupied molecular orbital (LUMO), respectively, and $\Delta E_{HOMO-LUMO}$ is the frontier orbital energy gap. E_{HOMO} is the ability of molecules to lose electrons (i.e., reduction), and E_{LUMO} is the ability of molecules to gain electrons (i.e., oxidation).[28] The frontier orbitals of m-NBO and BX are primarily concentrated at -NOO-, -COO-, and S. The regions of the molecule with high HOMO density have relatively loose outer electrons, which indicates that the electrons can transfer from sulfur atoms to metal species on the mineral surface to form covalent bonds.[29,30] This indicates that the sulfur atoms are the active centers of these molecules, which is consistent with the microflotation experimental results. Figure 8 shows that the nitro group is coplanar with the benzene ring to form a conjugated system. The nitro group has strong electron withdrawal properties, which attracts electrons from the conjugated system to move to the nitro group and reduces the electron cloud density of the benzene ring. m-NBO had E_{LUMO} = −5.07 kJ/mol. As per the frontier orbital theory, m-NBO has a certain degree of oxidation, which allows it to act as an inhibitor. A smaller absolute value for $\Delta E_{HOMO-LUMO}$ shows stronger activity and easier interaction between molecules. This indicates that m-NBO easily adsorbs on mineral surfaces.

Table 3. Frontier Orbital of Each Reagent

Reagent	E_{HOMO} (kJ·mol^{-1})	E_{LUMO} (kJ·mol^{-1})	$\lvert\Delta E_{HOMO-LUMO}\rvert$
m-NBO	0.88	−5.07	5.95
NaBX	13.07	−1.98	15.05

2.4.2. Adsorption Energies. Figure 9 shows the adsorption energies of xanthate on the Py (100) and Apy (001) surfaces with different reagents. NH_4^+ and m-NBO had little effect on the Py surface, which increased the effect of the collector BX. NH_4^+ and m-NBO had a greater effect on the Apy surface; therefore, they competed with BX for adsorption. This reduced the adsorption of BX on Apy and inhibited its floatability. The adsorption energy of xanthate was greater on the Py surface

https://doi.org/10.1021/acsomega.1c06902
ACS Omega 2022, 7, 6302−6312

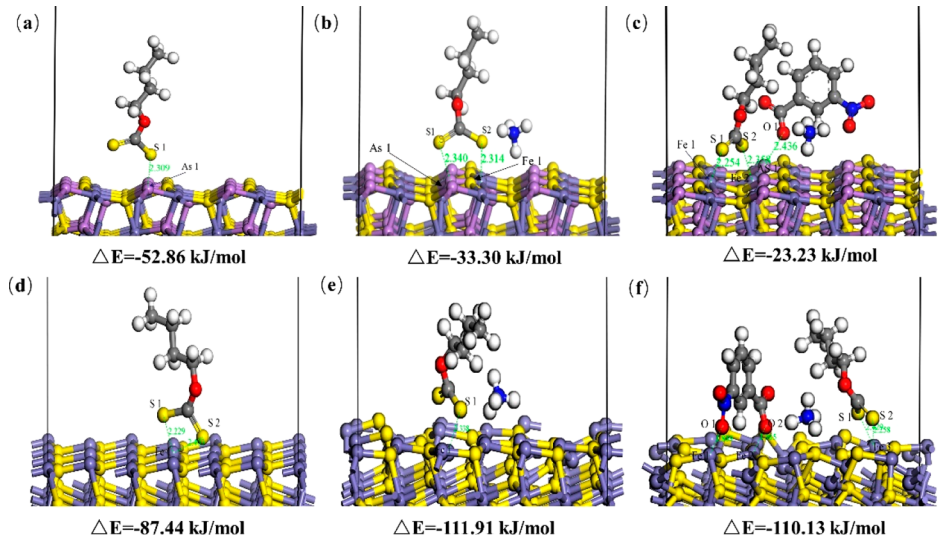

Figure 9. Total energy and adsorption energy of the reagent molecules: adsorptions of (a) BX, (b) NH_4^+, and BX and (c) NH_4^+, m-NBO, and BX on Apy; adsorptions of (d) BX, (e) NH_4^+, and BX and (f) NH_4^+, m-NBO, and BX on Py.

(ΔE = −52.86 kJ/mol) than on the Apy surface (ΔE = −87.44 kJ/mol), which indicates that BX possibly adsorbed onto the Py surface. When NH_4^+ reacted with Py (ΔE = −111.91 kJ/mol) and Apy (ΔE = −33.30 kJ/mol), NH_4^+ reduced the adsorption of BX on the Apy surface. The addition of m-NBO led to competitive adsorption between m-NBO and BX, which reduced the adsorption of BX on the Apy surface (ΔE = −23.23 kJ/mol) but had almost no effect on the Py surface (ΔE = −110.13 kJ/mol). Thus, these results demonstrate how the selective adsorption of Apy and Py could be achieved.

To summarize, the adsorption energy results demonstrated that xanthate more easily adsorbs on the Py surface. The addition of NH_4^+ reduced the adsorption energy of BX on the Apy surface compared with that on the Py surface. The addition of m-NBO did not affect the adsorption energy of BX on the Py surface but reduced the adsorption energy on the Apy surface. This shows that the combined action of NH_4^+ and m-NBO reduced the adsorption of BX on the Apy surface and inhibited its floatability.

2.4.3. Charge Density Difference. The electronic structure information of flotation reagents adsorbed on the crystal planes of minerals is quite significant for understanding the electron transfer and chemical bond properties after adsorption. Calculation of the charge density difference is an effective method for analyzing the electronic structure.[31] The electron flow direction before and after adsorption can be intuitively obtained by calculating the charge density difference. The charge density difference diagram is obtained by subtracting the charge densities after bonding and before bonding. Table 4 shows the Mulliken populations of related atoms after a flotation reagent adsorbed on the mineral surface. The average Mulliken population distributions of the atoms and bonds of Py and Apy for different systems can be used to explain the types of charge transfer and bond formation. Figure 10 shows the plot of the charge density differences of BX, NH_4^+, and m-NBO molecules on Py and Apy planes; the red area is electron scarcity, the blue area is electron enrichment, and the white area is no change in the electron density. The Py + BX system had populations of 0.46 (S1−Fe1) and 0.36 (S2−Fe1). The addition of NH_4^+ reduced the population of S2−Fe1 to 0.35 and, thus, enhanced the ionicity of the system.[32] The addition

Table 4. Changes in the Mulliken Charge Population for Apy and Py after the Adsorption of BX, NH_4^+, and m-NBO

Type	Atomic bond	Population	Distance (Å)
Apy + BX	S1−As1	0.48	2.04
Apy + NH_4^+ + BX	S1−As1	0.42	2.34
	S2−Fe1	0.45	2.31
Apy + NH_4^+ + m-NBO + BX	S1−Fe1	0.53	2.25
	S2−Fe2	0.46	2.35
Py + BX	S1−Fe1	0.46	2.23
	S2−Fe2	0.36	2.40
Py + NH_4^+ + BX	S2−Fe1	0.35	2.24
Py + NH_4^+ + m-NBO + BX	S1−Fe3	0.29	2.42
	S2−Fe2	0.37	2.25
	O1−Fe1	0.41	1.88
	O2−Fe2	0.40	1.96

m-NBO significantly reduced the population and, thus, increased the ionicity further.

In Figure 10, the red and blue patterns for BX show that many electrons moved from the outside of S1 and transferred to Fe ions; this is consistent with the weak electronegativity of Fe ions and their weak electron binding ability. The larger and darker red area in Figure 10(d) compared with Figure 10(a) shows that Fe1 transferred more electrons to S1 and, thus, had a stronger interaction. The results of the Mulliken population analysis were consistent. When NH_4^+ was added to the system, additional electrons were transferred from the outside of S1 to Fe. In Figure 10(b), Fe1 had a larger and lighter red area, which indicates that additional electrons were transferred to S1 and, thus, represents a stronger interaction. However, Figure 10(e) shows no obvious red area on the surface. The addition of NH_4^+ to the Apy surface weakened the ability of As1 and Fe1 to transfer electrons to S1, which reduced the effect of the collector BX. Adding m-NBO as shown in Figure 10(c) caused NH_4^+ to strongly interact with the Py surface. In Figure 10(f), the periphery of S1 is white, which indicates almost no change in the electron density; however, the periphery of m-NBO shows a more obvious red. These results show that m-NBO interacts with the Apy surface, which reduces the effect of the collector BX and, thus, inhibits the floatability of Apy.

https://doi.org/10.1021/acsomega.1c06902
ACS Omega 2022, 7, 6302−6312

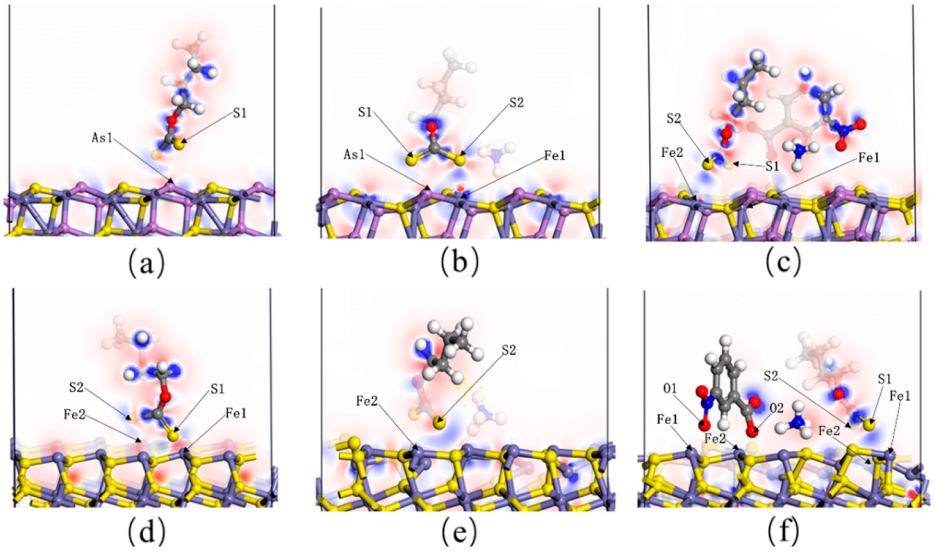

Figure 10. Front view of Mulliken charges when treatment reagents adsorb on the surfaces of Py (100) and Apy (001): Charge density differences when (a) BX, (b) NH_4^+, and BX and (c) NH_4^+, m-NBO, and BX adsorb on Apy; charge density differences when (d) BX, (e) NH_4^+, and BX and (f) NH_4^+, m-NBO, and BX adsorb on Py.

Table 5. Chemical Element Analyses of Apy and Py

	Element content (wt %)										
	Fe	As	S	Si	Zn	Al	Ca	Mg	Mn	K	P
Apy	34.93	47.12	14.88	1.37	0.64	0.51	0.48		0.03	0.03	0.01
Py	48.85		46.92	1.90		1.53	0.19	0.11		0.46	0.04

3. CONCLUSIONS

Both experiments and quantum chemistry were used to evaluate the effects of m-NBO and NH_4^+ on the floatability of Py and Apy. The microflotation experimental results demonstrated that the combined action of NH_4^+ and m-NBO can achieve the selective inhibition of Apy and Py. Zeta potential analysis shows that NH_4^+ reduced the surface potential of Apy but had little effect on Py. In an alkaline environment, m-NBO had a weak inhibitory effect on the Py surface when combined with NH_4^+. In the case of Apy, the combined action of m-NBO and NH_4^+ occupied active sites on the mineral surface, which significantly reduced the adsorption of BX and inhibited the floatability of Apy.

The primary reactive site of BX was the S atom, and the primary reactive site of m-NBO was the O atom. The primary activation site on the mineral surface was Fe. The Py surface had a significantly greater ΔE (110.13 kJ/mol) than BX (ΔE = 87.44 kJ/mol) after interacting with m-NBO and NH_4^+. This shows that m-NBO and NH_4^+ did not affect the BX adsorption capacity of the Py surface, which indicates that m-NBO had a weak inhibitory effect on Py. The Apy surface had a significantly smaller ΔE (23.23 kJ/mol) than BX (ΔE = 52.86 kJ/mol) after interacting with m-NBO and NH_4^+. This shows that m-NBO and NH_4^+ reduced the BX adsorption capacity of the Apy surface, which indicates that m-NBO had a strong inhibitory effect on Apy.

The Mulliken population analysis confirmed that the charge density differences on the Apy surface did not considerably change with the addition of NH_4^+ and m-NBO. These results confirmed those increased after the action of NH_4^+. O and S were reported to affect the activity and reactivity of flotation reagents on the mineral surface.

In the flotation process, multiple agents interact with each other, and the synergistic effect is widespread. For example, xanthate is partially oxidized into dixanthate and then coadsorbed to the mineral surface, which improves the flotation index. However, not all agents can improve the flotation index. Attention should be given to eliminate this adverse synergy effect, and this is not conducive to flotation. Furthermore, the mixing of foaming agents and collectors for sulfide minerals and fine flotation should be strengthened, and research on the mixed use of foaming agents should continue.

4. MATERIALS AND METHODS

4.1. Materials. Mineral samples were obtained from the Chifeng polymetallic sulfide deposit in Inner Mongolia, China.

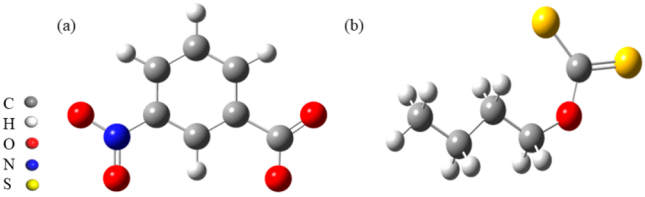

Figure 11. Molecular structures of flotation reagents: (a) m-NBO and (b) BX.

The mineral samples were manually selected, crushed, ground with agate, and sieved. Microflotation experiments were performed with 38−75 μm sized, and FTIR and zeta potential measurements were performed with 20−38 μm sized. Table 5 presents the chemical element analyses of ore samples used in this study: arsenopyrite (Apy) and pyrite (Py). The Apy

https://doi.org/10.1021/acsomega.1c06902
ACS Omega 2022, 7, 6302−6312

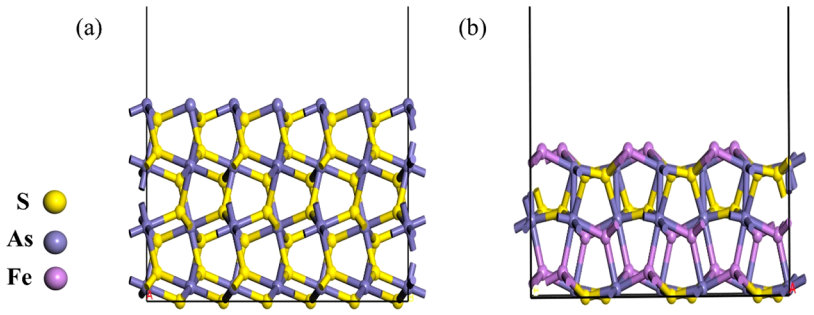

Figure 12. Optimized unit cell models: (a) Py and (b) Apy.

samples had a purity of 96.93%, whereas the Py samples had a purity of 95.66%.

In this study, different chemical reagents with different functions were used to evaluate their effects and interactions with each other. Analytically pure sodium *m*-nitrobenzoate (m-NBO) produced by Shanghai Macleans Biochemical Co., Ltd. (Shanghai, China) was selected as an inhibitor, whereas analytically pure ammonium chloride (NH_4^+) was selected as an activating reagent. Butyl xanthate (BX) with a purity of >85% from Zhuzhou Flotation Plant (Zhuzhou, China) was selected as the collector. Terpineol oil provided by Tangshan Jiesde Technology Co., Ltd. (Tangshan, China) was selected as the foaming agent. Furthermore, other reagents, including sodium hydroxide (NaOH) and hydrochloric acid (HCl), were analytically pure. Deionized water (resistivity: 18.2 MΩ) was used for all experiments and analyses.

4.2. Methods. *4.2.1. Microflotation Experiments.* Microflotation experiments were performed using a 40 mL flotation cell machine on 2 g ore samples. The flotation behaviors of Apy and Py were examined with different slurry systems under different pH conditions. Before each test, the mineral surface was cleaned by ultrasonication for 5 min. The pH was measured and adjusted as necessary using NaOH and HCl. Various reagents were then added as necessary: NH_4^+, m-NBO, and/or BX, followed by terpineol oil. After 2 min of flotation, the floating and sinking products were collected.

For the separation test of the artificial mixed minerals, 2 g of mixed mineral powders (1.5 g of pyrite and 0.5 g of arsenopyrite) was used. The test flow was the same as that of the single-mineral flotation.

Each flotation test was conducted under the same conditions three times. The recovery of products can then be expressed as follows:[33]

$$R = \frac{m_1}{m_1 + m_2} \times 100\% \quad (1)$$

where R is the recovery, m_1 is the mass of the floating product, and m_2 is the mass of the nonfloating product.

4.2.2. Zeta Potential Measurements. The zeta potential was measured using a Zetasize Nano ZS680 (Malvern, U.K.) zeta analyzer instrument. Suspensions (0.01% mass fraction) of a small amount of mineral sample in a 1×10^{-3} M KCl background electrolyte solution were dispersed in a beaker and magnetically stirred for 6 min at the desired pH. After 20 min of settling, the pH of the suspension was measured, and the supernatant was collected for zeta potential measurement. Tests were conducted thrice under the same conditions, and the average and standard deviation were calculated.[34]

4.2.3. FTIR Spectroscopy. FTIR spectroscopy was performed using a Nicolet IS 10 Fourier transform infrared spectrometer from Thermo Fisher Scientific (Waltham, MA, U.S.A.). The diffuse reflection approach (30 scans, resolution: 2 cm^{-1}) was utilized at room temperature (25 °C). Spectra were collected in the absorption band range 400−4000 cm^{-1}. Samples were prepared by adding 1.0 g of pure mineral particles (−38 μm in size) in 40 mL of deionized water as per the desired reagent scheme. After conditioning for 30 min, the suspension was filtered, and the filter cake was washed three times with deionized water at pH 6.5. Then, the filter cake was dried in a vacuum oven at 25 °C. After completely evaporating the moisture, 1 mg of dry solid was mixed with 100 mg of spectroscopy-grade KBr for analysis.[35]

4.3. Models and Computational Details. Under alkaline conditions, m-NBO and BX primarily exist in the form of anions. Therefore, this study primarily focused on modeling the anion form of these reagents. GaussView 6.0 was used to build molecular models of m-NBO[36] and BX, as shown in Figure 11. The package Gaussian 09 at the B3LYP functional and 6-311G^{+2} (d, p) basis set was used to optimize the geometry of molecular structures.[37,38]

Density functional theory (DFT) has been confirmed to be one of the most accurate methods for calculating the electronic structure of solids.[39,40] DFT simulations were performed by using the CASTEP module of Materials Studio 2017, and the Ultrasoft pseudopotential method was used for calculation. The periodic unit cell parameters of Py and Apy were obtained from the crystal structure database. The calculated lattice parameters were closest to the experimental results when the generalized gradient approximation (GGA-PBE) was used. Thus, the GGA-PBE functional was selected for subsequent calculations.[41] The DFT-D correction was applied to eliminate the effect of dispersion. The DFT calculations demonstrated that the most exposed dissociation planes for Py and Apy were (100)[42] and (001),[43] respectively. Figure 12 shows the resulting optimized unit cell models. To eliminate the influence between mirror molecules, the final supercell sizes of Py and Apy were 17.21 × 17.01 × 40 $Å^3$ and 16.25 × 16.25 × 40 $Å^3$, respectively. The atomic charges were determined as per Mulliken population analysis.[44] The plane wave cutoff energy was set to 500 eV for calculations. The Broyden−Fletcher−Goldfarb−Shanno (BFGS) algorithm[45] was used to optimize the models. The self-consistent field (SCF) convergence criterion was 2×10^{-6} eV/atom, the interatomic force was 0.05 eV/A, and the total change in energy of the system was 2×10^{-5} eV/atom. Point K was set to Gamma. All calculations were performed under periodic conditions. The adsorption energy reflects the acting intensity of a reagent, which can be calculated as follows:

$$E_{ads} = E_{ads/s} - (E_{ads} + E_s) \quad (2)$$

https://doi.org/10.1021/acsomega.1c06902
ACS Omega 2022, 7, 6302−6312

where $E_{ads/s}$ is the adsorption energy, E_{ads} is the total energy of Py (100) and Apy (001), and E_s is the energy of the adsorbent.

AUTHOR INFORMATION

Corresponding Authors

Bozeng Wu − *School of Chemical and Environmental Engineering, China University of Mining and Technology-Beijing, Beijing 100083, China; National Engineering Laboratory for Efficient Utilization of Indium and Tin Resources, Liuzhou 545000, China;* orcid.org/0000-0002-7181-0620; Email: wubz998@163.com

Jiushuai Deng − *School of Chemical and Environmental Engineering, China University of Mining and Technology-Beijing, Beijing 100083, China; Engineering Technology Research Center for Comprehensive Utilization of Rare Earth, Rare Metal and Rare-Scattered in Non-ferrous Metal Industry and Key Laboratory of Separation and Processing of Symbiotic-Associated Mineral Resources in Non-ferrous Metal Industry, CUMTB, Beijing 100083, China*; Email: jsdeng@cumtb.edu.cn

Hongxin Qiu − *School of Chemical and Environmental Engineering, China University of Mining and Technology-Beijing, Beijing 100083, China; National Engineering Laboratory for Efficient Utilization of Indium and Tin Resources, Liuzhou 545000, China;* orcid.org/0000-0002-9304-0022; Email: qiuhx0919@163.com

Authors

Xiaohao Sun − *School of Chemical and Environmental Engineering, China University of Mining and Technology-Beijing, Beijing 100083, China; National Engineering Laboratory for Efficient Utilization of Indium and Tin Resources, Liuzhou 545000, China*

Mingzhen Hu − *School of Chemical and Environmental Engineering, China University of Mining and Technology-Beijing, Beijing 100083, China; National Engineering Laboratory for Efficient Utilization of Indium and Tin Resources, Liuzhou 545000, China*

Jiaozhong Cai − *School of Chemical and Environmental Engineering, China University of Mining and Technology-Beijing, Beijing 100083, China*

Xiaoli Jin − *School of Chemical and Environmental Engineering, China University of Mining and Technology-Beijing, Beijing 100083, China*

Hongyang Xu − *School of Chemical and Environmental Engineering, China University of Mining and Technology-Beijing, Beijing 100083, China*

Complete contact information is available at: https://pubs.acs.org/10.1021/acsomega.1c06902

Funding

This work was supported by the financial support of the National Natural Science Foundation of China (no. 51764022), Fok Ying Tong Education Foundation (no. 161046), and Central Universities Basic Research Funds of China (no. 2020XJHH04).

Notes

The authors declare no competing financial interest.

ACKNOWLEDGMENTS

The authors thank Qingping Wu for her contributions to this article.

REFERENCES

(1) Li, Y. Q.; He, Q.; Chen, J. H.; Zhao, C. H. Electronic and chemical structures of pyrite and arsenopyrite. *J. Mineralogical Magazine* **2015**, *79*, 1779−1789.

(2) Guo, L.; Hu, Z. Q.; Du, Y. G.; Zhang, T. C.; Du, Dy Mechanochemical activation on selective leaching of arsenic from copper smelting flue dusts. *J. Journ of Hazardous Materials* **2021**, *414*, 125436.

(3) Bruckard, W.J.; Davey, K.J.; Jorgensen, F.R.A.; Wright, S.; Brew, D.R.M.; Haque, N.; Vance, E.R. Development and evaluation of an early removal process for the beneficiation of arsenic-bearing copper ores. *Miner. Eng.* **2010**, *23*, 1167−1173.

(4) Liu, J.; Zhou, L.; Dong, F. Q.; Hudson-Edwards, K. A. Enhancing As(V) adsorption and passivation using biologically formed nano-sized FeS coatings on limestone: Implications for acid mine drainage treatment and neutralization. *Chemosphere* **2017**, *168*, 529.

(5) Park, I.; Higuchi, K.; Tabelin, C. B.; Jeon, S.; Ito, M.; Hiroyoshi, N. Suppression of arsenopyrite oxidation by microencapsulation using ferric-catecholate complexes and phosphate. *Chemosphere* **2021**, *269*, 129413.

(6) Khoso, S. A.; Hu, Y.; Tian, M.; Gao, Z.; Sun, W. Evaluation of green synthetic depressants for sulfide flotation: Synthesis, characterization and floatation performance to pyrite and chalcopyrite. *Sep. Purif. Technol.* **2021**, *259*, 118138.

(7) Zhou, G. Y.; Li, W. J.; Chen, Y.; Song, Y. S. Study on Recovery of Lead-Zinc Tailing Ore by Electrochemical Flotation. *J. Applied Mechanics and Materials* **2014**, *675−677*, 1451−1454.

(8) Ahmadi, M.; Gharabaghi, M.; Abdollahi, H. Effects of type and dosages of organic depressants on pyrite floatability in microflotation system. *J. Advanced Powder Technology* **2018**, *29*, 3155−3162.

(9) Liu, S. Q.; Tong, X.; Lan, Z. Y.; Ji, C. C. Rejection of Arsenopyrite in a High As-Containing Pyrite Concentrate by Inorganic Depressants. *Adv. Mater. Res.* **2012**, *496*, 403−406.

(10) Xiong, D. L.; Hu, Y. H.; Qing, W. Q.; He, M. F. Synthesis of glycerine-xanthate and its depressing mechanism in separation of marmtite from arsenopyrite. *J. Central South Univ. Technol.* **2006**, *13*, 678−682.

(11) Kenzhaliev, B. K.; Tusupbaev, N. K.; Medyanik, N. L.; Semushkina, L. Understanding the Physico-Chemical and Flotation Characteristics of Composite Flotation Reagents. 2019, *17*, DOI: DOI: 10.18503/1995-2732-2019-17-3-4-11.

(12) Yan, S.; Zhang, J. Q.; Diao, W. Z. Flotation Reagent Progress and Application Overview. *Appl. Mech. Mater.* **2013**, *441*, 76−79.

(13) Lee, K.; Archibald, D.; McLean, J.; Reuter, M.A. Flotation of mixed copper oxide and sulphide minerals with xanthate and hydroxamate collectors. *Miner. Eng.* **2009**, *22*, 395−401.

(14) Marabini, A. M.; Ciriachi, M.; Plescia, P.; Barbaro, M. Chelating reagents for flotation. *J. Minerals Engineering* **2007**, *20*, 1014−1025.

(15) Li, Y. J.; Xiong, F.; Lan, Y. Z. Synergistic Effect in the Flotation and Extraction of Minerals[C]//Advanced Materials Research. *Trans Tech Publ* **2013**, *868*, 451−454.

(16) Janetski, N. D.; Woodum, S. I.; Woods, R. An electrochemical investigation of pyrite flotation and depression. *Int. J. Miner. Process.* **1977**, *4*, 227−239.

(17) Chanturia, E. L.; Ivanova, T. A.; Zimbovsky, I. G. Improved selectivity of sulfide ore flotation. *J. Min. Sci.* **2013**, *49*, 132−137.

(18) Qiu, H. X.; Chen, Z. R.; Wang, G. H. Effect of Dodecyl Trimethyl Ammonium Bromide on the Migration of Water Molecules in the Pores of Lignite: An Experimental and Molecular Simulation Study. *J. ACS Omega* **2020**, *5*, 25456−25466.

(19) Chen, Z. R.; Li, Y. H.; Chen, C.; Sun, X.; Liu, W. G. Gas Hydrate Surface with Different Surfactant Coverages. *J. Phys. Chem. C* **2021**, *125*, 16378−16390.

(20) Qiu, H.; Deng, J.; Wu, B.; Sun, X.; Cai, J.; Chen, Z.; Xu, H. Study on the microscopic aggregation behavior of lignite molecules in water. *Colloids Surf. A* **2022**, *637*, 128194.

(21) Yang, G.; Yang, G. W.; Xu, H.; Hou, W. H. Flotation Mechanism and Molecular Design of Mercaptobenzo Flotation Reagents. *Acta Chim. Sin.* **2004**, *62*, 153−159.
(22) Chen, J. A.; Liu, J. Research on Mineral Processing Technical of a Gold Ore[C]//Advanced Materials Research. *Trans. Tech. Publ.* **2012**, 361−363. DOI: 10.4028/www.scientific.net/AMR.361-363.311.
(23) Kenji, O. N. O.; Takeuchi, T.; Kozo, S. Effect on Some Ammonium Salts on the Flotation of Iron Sulphide Minerals. *Sci. Rep. Res. Instit., Tohoku Univ., Ser. A* **1960**, *12*, 62−79.
(24) Li, W. Z.; Qin, W. Q.; Sun, W.; Qiu, G. Z. Electrodeposition of dixanthogen (TETD) on pyrite surface. *Trans. Nonferrous Met. Soc. China* **2007**, *17*, 154−158.
(25) Shanghai Institute of Organic Chemistry of CAS. Chemistry Database[DB/OL]. http://www.organchem.csdb.cn. [1978-2021].
(26) Shen, Y.; Nagaraj, D. R.; Farinato, R.; Somasundaran, P.; Tong, S. Decomposition of Flotation Reagents in Solutions Containing Metal Ions. Part II: Interactions between Xanthate and Metal Ions in Solutions. *Miner. Eng.* **2019**, *139*, 105832.
(27) Xiaojun, X.; Kelebek, S. Activation of xanthate flotation of pyrite by ammounium salts following it's depression by lime. *Dev. Miner. Process.* **2000**, *13*, C8b-43−C8b-50.
(28) Zhang, J. F.; Hu, H. Y.; Xu, J.; Wang, D. Quantum chemical calculation on properties of phenoxy acetic acids depressants. *Chin. J. Nonferrous Met.* **2004**, *8*, 1437−1441.
(29) Wang, D. *Flotation reagents: applied surface chemistry on minerals flotation and energy resources beneficiation*; Springer, 2016.
(30) Liu, G.; Yang, X.; Zhong, H. Molecular design of flotation collectors: A recent progress. *J. Advances in colloid and interface science* **2017**, *246*, 181−195.
(31) Li, R.; Zhang, Y.; Li, M.; Wang, Y. Adsorption behaviors of NH3 and HCl molecules on Fe-based crystal planes: A DFT study. *Chem. Eng. Sci.* **2021**, *246*, 116976.
(32) Lingam, C. B.; Babu, K. R.; Tewari, S. P.; Vaitheeswaran. Structural, electronic, bonding, and elastic properties of NH3BH3: A density functional study. *J. Comput. Chem.* **2011**, *32*, 1734−1742.
(33) Cui, Y. F.; Jiao, F.; Qin, W. Q.; Dong, L. Y.; Wang, X. Synergistic depression mechanism of zinc sulfate and sodium dimethyl dithiocarbamate on sphalerite in Pb−Zn flotation system. *J. Trans. Nonferrous Met. Soc. Chin.* **2020**, *30*, 2547−2555.
(34) Wang, J. J.; Gao, Z. Y.; Gao, Y. S.; Hu, Y. H.; Sun, W. Flotation separation of scheelite from calcite using mixed cationic/anionic collectors. *Miner. Eng.* **2016**, *98*, 261−263.
(35) Zeng, G. S.; Ou, L. M.; Zhang, W. C.; Zhu, Y. T. Effects of Sodium Alginate on the Flotation Separation of Molybdenite From Chalcopyrite Using Kerosene as Collector. *J. Front Chem.* **2020**, *8* DOI: 10.3389/fchem.2020.00242.
(36) Janczak, J. Structure and phase transition in 1-(diaminomethylene)thiouron-1-ium m-nitrobenzoate monohydrate and the structure of its anhydrous deuterated analogue. *J. Mol. Struct.* **2021**, *1230*, 129626.
(37) Lee, K.; Murray, E. D.; Kong, L.; Lundqvist, B. I.; Langreth, D. C. Higher-accuracy van der Waals density functional. *Phys. Rev. B* **2010**, *82*, No. 081101.
(38) Witte, J.; Goldey, M.; Neaton, J. B.; Head-Gordon, M. Beyond Energies: Geometries of Nonbonded Molecular Complexes as Metrics for Assessing Electronic Structure Approaches. *J. Chem. Theory Comput.* **2015**, *11*, 1481−1492.
(39) Li, Z. Y.; He, W.; Yang, J. L. Recent progress in density functional theory and its numerical methods. *J. Prog. Chem.* **2005**, *17* (2), 192−202.
(40) Ejuh, G. W.; Fonkem, C.; Tadjouteu Assatse, Y.; Yossa Kamsi, R. A.; Nya, T.; Ndukum, L. P.; Ndjaka, J. M. B. Study of the structural, chemical descriptors and optoelectronic properties of the drugs Hydroxychloroquine and Azithromycin. *Heliyon* **2020**, *6* (8), e04647.
(41) Xian, H. Y.; Wu, X.; Zhu, J. X.; Du, R. X.; Wei, J. M.; Zhu, R. L.; He, H. P. Environmental-sulfur-controlled surface properties of pyrite: a first principles PBE plus U study. *J. Phys. Chem. Miner.* **2021**, *48*, DOI: 10.1007/s00269-021-01145-7.
(42) Andersson, K.; Nyberg, M.; Ogasawara, H.; Nordlund, D.; Kendelewicz, T.; Doyle, C. S.; Brown, G. E.; Pettersson, L. G. M.; Nilsson, A. Experimental and theoretical characterization of the structure of defects at the pyrite FeS 2 (100) surface. *Phys. Rev. B* **2004**, *70*, 19.
(43) Silva, J. C. M.; De Abreu, H. A.; Duarte, H. A. Electronic and structural properties of bulk arsenopyrite and its cleavage surfaces−a DFT study. *RSC Adv.* **2015**, *5*, 2013−2023.
(44) Yang, X. L.; Albijanic, B.; Liu, G.; Zhou, Y. Structure−activity relationship of xanthates with different hydrophobic groups in the flotation of pyrite. *J. Miner. Eng.* **2018**, *125*, 155−164.
(45) Ahmoum, H.; Boughrara, M.; Su'ait, M. S.; et al. Monte Carlo and Density Functional Theory investigation on the Magnetic Nature Properties of MnB2. *J. Environ. Eng. Sci.* **2020**, *6*, 429−435.

https://doi.org/10.1021/acsomega.1c06902
ACS Omega 2022, 7, 6302−6312